Research Square

Preprints are preliminary reports that have not undergone peer review.
They should not be considered conclusive, used to inform clinical practice,
or referenced by the media as validated information.

Ignition Dynamics of Vegetation in Electrical Faults: Multimodal Insights in Wildfire Mitigation

Rui Li

rui.li@vu.edu.au

Victoria University

Cagil Ozansoy

Victoria University

Research Article

Keywords: Power line ignition, High-impedance fault, Firebrand, Ember detection, Vegetation flammability

Posted Date: November 20th, 2026

DOI: https://doi.org/10.21203/rs.3.rs-11541377/v1

License: This work is licensed under a Creative Commons Attribution 4.0 International License.
Read Full License

Additional Declarations: No competing interests reported.

Ignition Dynamics of Vegetation in Electrical Faults: Multimodal Insights in Wildfire Mitigation

Abstract

Vegetation contact with energised power lines is a major cause of wildfire. This study analyses 499 staged phase-to-earth High-Impedance Fault (HIF) tests on twelve vegetation species common in Victorian powerline corridors (seven native Australian, five introduced), from the public Vegetation Conduction Ignition Testing programme. Fault current was recorded at 100 kSa/s and time-stamped to 48 fps video, and supply was removed when the current reached a pre-set cut-off of 0.5, 1, or 2 A. An HSV colour-space and motion-differencing pipeline with plasma-referenced normalisation provides an optical index of flying-ember activity, binary logistic regression models the fire/no-fire outcome, and a near-white pixel metric (Cumulative Flame Intensity) identifies flame breakout. The pre-set cut-off current (positive) and the initial fault current (negative) are the significant predictors of fire (in-sample AUC 0.82); the observed fire rate rises from 11% at a 0.5 A cut-off to 65% at 2 A, and moisture content is not a significant predictor. Because cut-off setting and exposure time cannot be separated in this design, the association does not show that lower protection settings would reduce ignitions in the field. Among fire-producing tests from ten species, time to first ember, ember duration, and peak single-frame ember count differ significantly between species, whereas total ember quantity does not; three provisional groupings of ember behaviour are described. The ember index was not validated against particle-level ground truth. In one representative test, ember bursts co-occur with elevated arc current volatility. The results provide species-resolved laboratory reference data for vegetation management and protection studies.

Keywords: Power line ignition, High-impedance fault, Firebrand, Ember detection, Vegetation flammability

1 Introduction

Wildfires initiated by electrical distribution faults represent a disproportionately severe subset of fire events, accounting for a significant share of catastrophic ignitions in Australia, California, and southern Europe Bilancia (2020); Muhs et al. (2021). When energised conductors contact or fall across vegetation, the resulting arc discharge can deposit enough thermal energy to ignite dry plant material, yet the low fault currents

characteristic of High-Impedance Faults (HIFs) frequently evade conventional overcurrent protection Cong et al. (2023). Vegetation can therefore ignite without the fault being detected, and experimentally grounded models of ignition under electrical fault conditions are needed.

Prior research has examined ignition thresholds for individual fuel types and has explored the electrical signatures of downed conductors, but few studies have integrated synchronised multimodal measurements across a diverse range of species found in Australian powerline corridors under controlled fault scenarios Gomes et al. (2020); Wunderlich et al. (2021). The heterogeneity of vegetation in wildfire-prone corridors, encompassing species that differ substantially in moisture content, morphology, and bulk density, motivates a comparative experimental approach.

This study addresses that gap through a new analysis of the publicly available dataset from the Victorian Vegetation Conduction Ignition Testing programme Marxsen (2015); Victorian Government (2016). In that programme, a purpose-built high-voltage test rig replicated both phase-to-earth (ph-to-e) and phase-to-phase (ph-to-ph) fault conditions at distribution voltages, and twelve species (seven native Australian and five introduced) were subjected to repeated staged faults. The present analysis uses the 499 valid ph-to-e tests on these species. The experiments were designed and conducted by the original test programme; the contribution of the present work lies in the synchronised optical–electrical analysis of the recorded data. Outcomes are characterised using two primary analytical methods, HSV-based flying-ember detection and binary logistic regression of the fire outcome, supported by a Cumulative Flame Intensity (CFI) signal used to identify flame breakout. Together, these methods describe the progression from initial arc contact through flame breakout to ember ejection.

The contributions of this work are threefold. First, we develop an HSV colour-space and motion-differencing algorithm with plasma-referenced normalisation. To the authors' knowledge, it provides the first image-based index of flying-ember activity from staged vegetation conduction faults. Normalising ember pixel area by the arc plasma area of the same recording supports cross-test comparison. Second, time-synchronised analysis of a representative ph-to-e test shows that ember burst episodes co-occur with periods of elevated RMS current volatility. Third, binary logistic regression identifies the pre-set cut-off current and the initial fault current as the strongest of the predictors tested, and five ember metrics are used to compare ten species and to propose three provisional ember risk profiles. These profiles can inform vegetation management prioritisation along power line corridors.

The remainder of this paper is structured as follows. Section 2 reviews relevant literature on vegetation fire dynamics, HIF detection, and electrical fault ignition. Section 3 describes the experimental setup and instrumentation. Sections 4–6 present the flame intensity, ember detection, and fire occurrence analyses, respectively. Section 7 compares ember generation across species. Section 8 gives the conclusions and implications for power line corridor risk management.

2 Literature Review

2.1 Fault Detection in Vegetation High-Impedance Faults

Research on Vegetation High-Impedance Faults (VeHIFs) has predominantly centred on the classification problem: determining whether a fault has occurred rather than characterising the temporal evolution of the fault and its consequences. Cong et al. Cong et al. (2023) studied the rapid identification of tree-contact faults by decomposing the electrical signature into three sequential stages (approach, contact, and separation) but acknowledged persistent challenges in detecting transient fault clearance events. Gomes et al. Gomes et al. (2020) applied sparse coding to extract discriminative patterns from voltage signals during VeHIFs, demonstrating that high-frequency components and high-speed sampling are essential for reliable detection. Similarly, Wunderlich et al. Wunderlich et al. (2021) developed DC protection schemes that monitor current and voltage ramp rates to detect high-impedance faults on rate-limited distribution networks, while Ashok and Yadav Ashok and Yadav (2021) diagnosed cross-country high-impedance faults on dual-circuit lines using wavelet packet energy features. A common limitation of these detection-oriented studies is that they treat the fault as a binary event (fault versus no-fault) and do not address what happens after fault inception, specifically whether and how vegetation ignites, how combustion develops over time, or what governs the transition from charring to sustained flame. More recent work has begun to bridge this gap. Yang et al. Yang et al. (2025) observed that leakage currents during tree faults follow a characteristic "rise–fall–rise" pattern as the vegetation dries and chars, which gives a time-resolved electrical signature of the pyrolysis process. The visual and thermal aspects of the ignition sequence, however, remain uncharacterised in the fault detection literature.

2.2 Arc Physics and Electrothermal Modelling of Vegetation Faults

The electrical arc in a vegetation fault is a highly nonlinear phenomenon whose behaviour is governed by contact impedance, vegetation material properties, and the applied voltage. Classical arc models, notably the Cassie and Mayr formulations, have been adapted to describe the dynamic characteristics of vegetation arcs. Jiang et al. Jiang et al. (2024) constructed an arc plasma simulation model based on magnetohydrodynamic (MHD) theory to study the dynamic development of arc grounding faults on 10 kV distribution lines, analysing the effects of moisture content, wind speed, and conductor type on arc temperature, morphology, and development characteristics. Their experiments further showed that the branch resistance passes through five stages as the fault develops, with the leakage current following these changes. Zhou et al. Zhou et al. (2025) extended this framework by proposing an arc grounding fault model that captures the entire process of tree-related faults through four distinct stages: arc initiation, moisture dispersion, multi-stage carbonisation, and breakdown. Using a four-parameter controlled arcing fault model fitted via particle swarm optimisation, they achieved greater than 98% of simulation points with less than 10%

relative error across 100,000 data samples from experimental tests on a 10 kV platform. Gao et al. Gao et al. (2024) proposed a dynamic geometry-dimension model of high-impedance arc faults, replacing the fixed arc length and diameter of the classical cybernetic arc model with time-varying values and fitting the model parameters by particle swarm optimisation. These modelling advances provide the theoretical basis for understanding how electrical energy is delivered to the vegetation, a prerequisite for explaining the subsequent combustion and ember generation processes that are the focus of the present study. A notable limitation of the arc modelling literature is its unidirectional focus: electrical parameters are used to predict thermal delivery to the vegetation, but the reverse pathway has not been systematically studied. This includes the influence of sustained combustion on arc characteristics through conductive smoke, localised temperature changes, and impedance evolution. This bidirectional coupling between combustion and arc behaviour represents an open research question.

2.3 Fire Spread Modelling and Vegetation Flammability

A parallel body of research has addressed wildfire ignition and spread from a combustion science perspective, largely independent of the electrical fault literature. Mell et al. Mell et al. (2007) established foundational physics-based flame spread models, demonstrating that radiative heat transfer dominates in grassland fires but becomes secondary to convective heating in fine fuel structures. Finney et al. Finney et al. (2015) linked buoyancy-driven flame instabilities to wildfire spread rates, showing that intermittent flame contact controls fire progression in many fuel types. Sahila et al. Sahila et al. (2023) provided a detailed comparative analysis of combustion dynamics across Mediterranean plant species, quantifying flammability metrics such as time to ignition, peak heat release rate, and flaming duration. These studies establish the physical principles governing vegetation combustion but do not consider the electrical arc as an ignition source. The energy delivery mechanism in a VeHIF, where an arc progressively heats and pyrolyses the vegetation, differs from the radiant or convective ignition scenarios assumed in wildfire spread models. This distinction matters because arc-driven ignition involves localised, high-intensity energy deposition that simultaneously dries, chars, and ignites the fuel, which may compress the pyrolysis timeline relative to natural fire scenarios.

2.4 Arc–Vegetation Interaction and Ignition Thresholds

The intersection of electrical arc behaviour and vegetation ignition has received comparatively limited attention. Bilancia Bilancia (2020) explored branching Lichtenberg discharge patterns in vegetation exposed to electrical discharges, while Muhs et al. Muhs et al. (2021) developed probabilistic models for wildfire ignition caused by power distribution lines, incorporating vegetation type and moisture content as key parameters. Marxsen Marxsen (2015) conducted a large experimental programme, staging hundreds of vegetation conduction ignition tests under code-red fire weather conditions and quantifying species-dependent arc energy thresholds for ignition. His work showed that ignition susceptibility varies substantially across species and is

governed by the interplay of moisture content, branch geometry, and arc energy delivery rate. Ozansoy and Sianaki Ozansoy and Sianaki (2024) subsequently used the same test programme to rank vegetation species by fire risk, examining species differences in the harmonic content of the fault current. Wang et al. Wang and Bocchini (2023) extended the analysis to dynamic conditions, demonstrating that wind-induced conductor swaying significantly reduces minimum vegetation clearance distances and increases flashover risk, a factor that static clearance models systematically underestimate during code-red weather. Machine learning-based approaches have also emerged for estimating ignition probabilities by integrating electrical fault data with environmental parameters Earth Science Technology Office (2020). Despite these advances, existing studies predominantly treat ignition as a threshold event without characterising the temporal dynamics of combustion development. These include the charring duration, flame growth rate, and the transition to sustained burning.

2.5 Ember Generation, Transport, and Quantification

In the context of elevated vegetation faults on distribution networks, the primary mechanism of fire initiation at ground level is the generation and transport of airborne embers (firebrands) from the ignition zone at conductor height. Tse and Fernandez-Pello Tse and Fernandez-Pello (1998) modelled the flight paths and burnout of hot metal particles and burning embers produced by power lines in high winds, showing that such particles can travel substantial distances before landing, and Hadden et al. Hadden et al. (2011) showed experimentally that the ignition of a fuel bed by a hot particle depends jointly on particle size and temperature. Manzello et al. Manzello et al. (2020) reviewed firebrand generation, combustion, and the ignition of recipient fuels in large outdoor fires. However, ember generation at the vegetation–conductor contact point during an electrical fault has not been measured. In the broader wildfire science literature, ember detection and measurement have advanced substantially. Zen et al. Zen et al. (2021) developed a field-deployable emberometer combining visible-spectrum and longwave infrared cameras to measure firebrand fluxes, geometries, and thermal conditions during wildland fires. Kim and Sunderland Kim and Sunderland (2019) demonstrated ember pyrometry using an inexpensive digital colour camera, achieving temperature measurements between 750 and 1070 °C with uncertainty of ±20 °C through a hybrid ratio/grayscale pyrometry technique. Hu et al. Hu et al. (2023) created the FireFly synthetic dataset for ember detection using computer vision, improving mean average precision by 8.57% relative to models trained exclusively on small real datasets. Thompson et al. Thompson et al. (2022) developed an acoustic-based method for quantifying firebrand production and transport from in-fire camera recordings. These studies show that image-based and multi-sensor ember detection is well developed for wildfires. None has been applied to ember generation from electrical faults, where the ignition geometry (a localised arc-vegetation contact point at conductor height), the energy source (an electrical arc rather than a propagating flame front), and the combustion dynamics (progressive charring under sustained electrical energy input) differ from the wildfire scenarios in the existing literature.

2.6 Research Gaps and Contributions of the Present Study

The preceding review identifies three gaps at the intersection of fault detection, combustion science, and wildfire risk assessment. First, existing studies treat vegetation ignition as a threshold event without characterising the temporal dynamics of combustion development, including the progression from initial charring through flame breakout to sustained burning and ember ejection. Second, ember generation at the fault itself has not been quantified for electrical distribution faults, despite embers being the primary mechanism of fire initiation at ground level during elevated vegetation faults. Third, the relationship between electrical fault parameters (initial fault current, cut-off current, fault duration) and combustion outcomes (flame intensity, ember production, ember duration) has not been systematically established across species. Drawing on the Vegetation Conduction Ignition Testing programme Marxsen (2015) and recent electrical signature literature Yang et al. (2025), three stages of ignition development are identified in VeHIF faults. In Stage-1 (contact development), the fault current rises as the plasma channel establishes between the conductor and vegetation, reaching an initial peak. In Stage-2 (moisture expulsion), the fault current declines as resistive heating expels moisture from the branch, progressively increasing the vegetation impedance. In Stage-3 (progressive charring), the dried vegetation begins to char, creating a carbonised conductive path that reduces impedance; sustained flames develop and cause pulsations in the fault current before it rises to large values as the flame front advances along the branch. In the test programme analysed here, supply was removed when the current reached a pre-set cut-off value, so the extent to which a fault progressed into Stage-3 before de-energisation was governed by that setting. This study addresses these gaps through a synchronised electrical–visual analysis of 499 staged faults, quantifying the associations between fault parameters and combustion outcomes, and introducing an optical index of flying-ember activity derived from a dedicated HSV colour-space pipeline with plasma-referenced normalisation.

3 Experimental Setup

The dataset analysed in this study comes from staged VeHIFs conducted for the "Vegetation Conduction Ignition Testing" project Marxsen (2015); the present work is a secondary analysis of the recorded electrical data and video. The twelve species tested were *Acacia mearnsii*, *Acacia melanoxylon*, *Acacia pycnantha*, *Acacia verticillata*, *Eucalyptus baxteri*, *Eucalyptus viminalis*, and *Pittosporum undulatum* (native Australian), and *Cotoneaster glaucophyllus*, *Fraxinus angustifolia*, *Pinus radiata*, *Salix* sp., and *Schinus molle* (introduced). Fig. 1 shows the test rig, which supported two parallel conductors for both ph-to-ph (22 kV) and ph-to-e (12.7 kV) operations for staged "branch touching wire" faults of diverse vegetation species. Code red fire weather conditions were simulated by keeping the ignition test area temperature at 45 °C and less than 25% relative humidity. A fan replicated "swirling" hot winds.

In each test, the fault current was measured continuously from fault inception. The initial fault current is the RMS current at the start of the fault, when the branch first conducts and before resistive heating alters its impedance; its level depends on

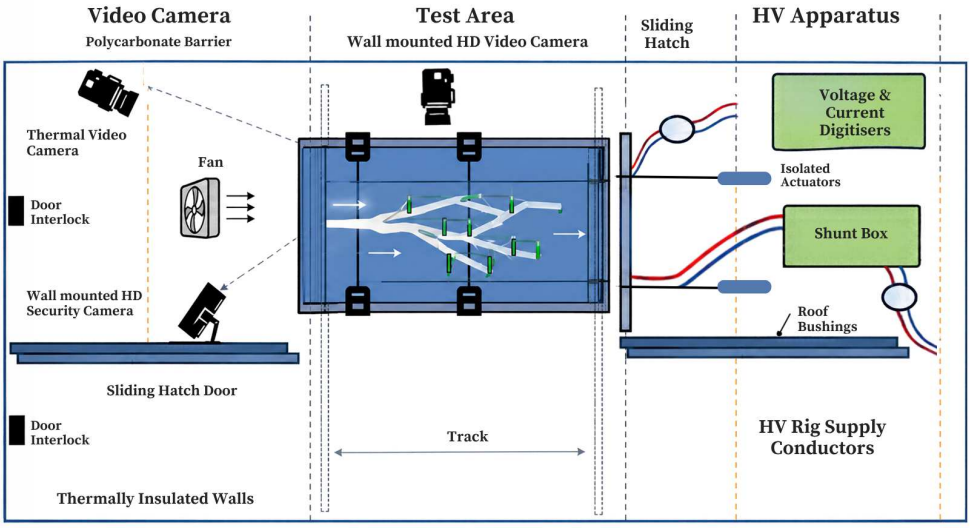


Fig. 1 Test rig schematic showing the test area, fan, cameras, conductors, and HV apparatus (adapted from Marxsen (2015)).

the moisture content, sap ionic content, and diameter of the branch Marxsen (2015). Consistent with this, initial current in the present dataset is positively correlated with moisture content ($r = 0.52$), branch conductivity ($r = 0.34$), and branch diameter ($r = 0.32$). After inception, the current typically took 10–15 s to build to its first peak Marxsen (2015). Branch moisture content was determined by the testing laboratory on a short length cut from the end of each sample immediately before the test and sealed for transport Marxsen (2015), and is reported as a percentage of sample weight (%wt.); across the 499 tests it ranged from 14 to 60% (median 37%). Where recorded, branch diameter at the contact point was typically 25–35 mm (median 30 mm). Supply was removed automatically when the current reached a pre-set cut-off value of 0.5, 1, or 2 A; the three settings were applied in approximately equal numbers of tests within each species. The cut-off current is therefore a test setting, chosen before each test and analogous to the pickup threshold of a protection device, rather than an outcome of the test; the duration of current application is the time taken for the current to reach this threshold. Combustion of the branch could continue after supply removal, and its persistence varied between species.

Fig. 2 shows the voltage/current measurement system. The voltage transducer was a 1.1-nF rated 24 kV Coupling Capacitor (CC) connected via an 11 m coaxial cable to a Capacitive Voltage Divider (CVD) with a 2000:1 voltage ratio at 50 Hz. The CVD output was sampled at 100 kSa/s with anti-alias filtering, providing a DC–50 kHz Low Frequency (LF) Voltage channel. Current recording employed a HiLo Test 0.2 Ω coaxial shunt sampled at 100 kSa/s, providing a DC–50 kHz LF Current channel Marxsen (2015). Relevant data and test videos are available at the Victorian Department website Victorian Government (2016).

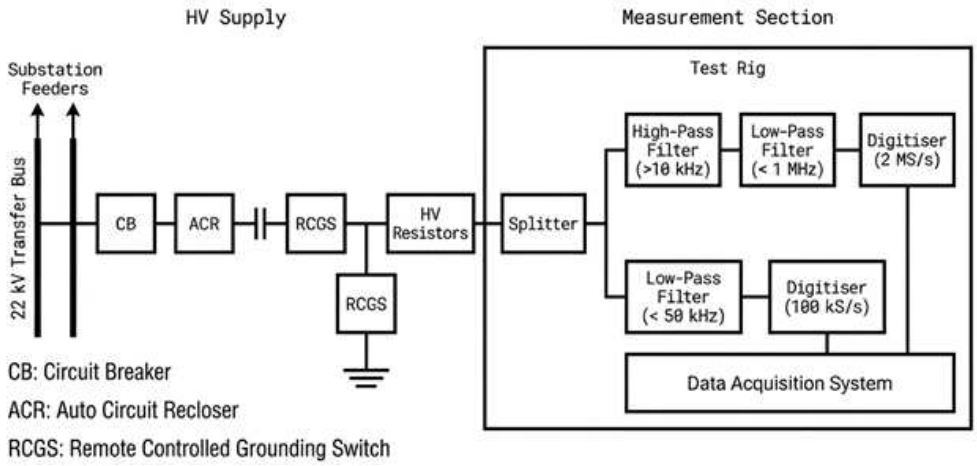


Fig. 2 Single-line diagram of the test rig and measurement system, including the ACR for current limiting, HV resistors, and sampling coupling. The measurement section (right) shows the electrical signal path.

Fire starts occur when ignition at height produces falling embers that ignite dry grass at ground level. Well-alight embers of significant size carry sufficient thermal capacity to initiate secondary ignition upon landing Marxsen (2015). Some tests were classified as no-fire despite branch charring, and some of these involved flashovers. Risk categorisation was based on whether a particular test was "fire-producing" or not under criteria defined in Marxsen (2015).

All 499 tests were conducted using the same enclosed laboratory setup with fixed artificial lighting, eliminating inter-test illumination variability. The camera was mounted at a fixed position and orientation for all tests, with the same focal length, aperture, and white balance settings maintained throughout the test programme. Video was recorded at 48 fps, verified before each test session. Automatic exposure compensation remained active during recording; its effect is corrected by the reference-frame normalisation described in Section 5. The electrical records were time-stamped to the video timeline, and all times reported in this paper are electrical-record times corrected to this common time base, with $t = 0$ s at the start of the current/voltage record unless stated as time after fault inception or energisation. At 48 fps, the timing resolution of optically detected events is one frame (20.8 ms). This controlled and repeatable optical configuration underpins the cross-test comparability of the pixel-based analyses presented in Sections 4 and 5.

The voltage and current measurement channels were calibrated prior to the test programme. The CVD ratio (2000:1 at 50 Hz) and the 0.2 Ω coaxial current shunt were verified against traceable standards. Electrical time series were sampled at 100 kSa/s on both channels with anti-alias filtering, providing consistent measurement bandwidth across all tests.

Fire occurrence (fire or no-fire outcome) and fire duration were recorded manually by a trained observer for each test at the time of testing, independently of the automated optical analysis. These manual records served as the ground-truth reference for

validating the timing of combustion events detected by the algorithms. They do not provide particle-level ground truth for ember detection, which was not available for this dataset; the ember metrics in Sections 5 and 7 are therefore reported as an optical activity index rather than a validated particle count. Where the algorithm-derived fire onset time or ember duration differed from the manually recorded value by more than 5%, the test was flagged for review. Tests for which no clear technical explanation could be identified (for example, camera obscuration or recording truncation) were excluded from the statistical analyses to prevent anomalous recordings from influencing the species comparisons. Of the 499 valid ph-to-e tests on the twelve species, 193 produced fire. The ember analysis (Section 7) uses 132 of these fire-producing tests, from ten species; the remaining 61 fire-producing tests were excluded because of missing data.

4 Relative Flame Intensity Analysis

A MATLAB script was developed to analyse the colour distribution in image frames extracted at 0.25 s intervals. Each frame is converted to a normalised RGB representation, and unique colour combinations are identified with occurrence frequencies computed. Colours appearing fewer than a prescribed minimum count are discarded to reduce noise and exclude spurious pixel values. The analysis focuses on near-white pixels, defined as those satisfying RGB ≥ 0.92 in all three channels simultaneously, thereby suppressing colour-biased reflections or sensor noise. Prior work on flame segmentation Zhao et al. (2023) has reported that intense flame regions exhibit RGB values exceeding approximately 230 in 8-bit encoding (RGB ≥ 0.90 normalised). A threshold of 0.92 was selected following sensitivity analysis across the range 0.90–0.95; the temporal trends of the resulting pixel count metric were insensitive to threshold variation within this range, indicating robustness of the flame breakout detection. The threshold operates as a detection criterion for sustained high-luminance emission rather than a photometrically calibrated intensity measurement.

The resulting near-white pixel counts are summed per frame, providing a quantitative representation of flame and arc development over time. For each test, the pixel count is normalised with respect to a baseline reference frame captured prior to flame development in the same sequence. The proposed analysis evaluates relative temporal changes in the spatial density of near-white pixels within each individual video sequence. This per-sequence normalisation suppresses uniform exposure adjustments and ensures the metric reflects relative flame evolution within a test independently of cross-test exposure differences; the method therefore remains robust to global exposure adaptation by the camera. Direct cross-test comparison of absolute CFI values is therefore not performed. Fig. 3 shows the pre-energisation baseline reference frame for test VT132, captured prior to fault inception and used for per-sequence normalisation. Fig. 4 presents the captured flame intensity state at 21.13 s into the ph-to-e fault alongside the corresponding electrical time-series for VT132 (*A. mearnsii*, moisture content 30.3%, 2-A_{rms} cut-off current). Visual flame breakout is detected 12.71 s after fault inception (approximately 16 s record time), with a Cumulative Flame Intensity of 1,698,660 pixel-frames at 21.13 s into the fault, where one pixel-frame represents one near-white pixel detected in one video frame at the 0.25 s sampling interval.

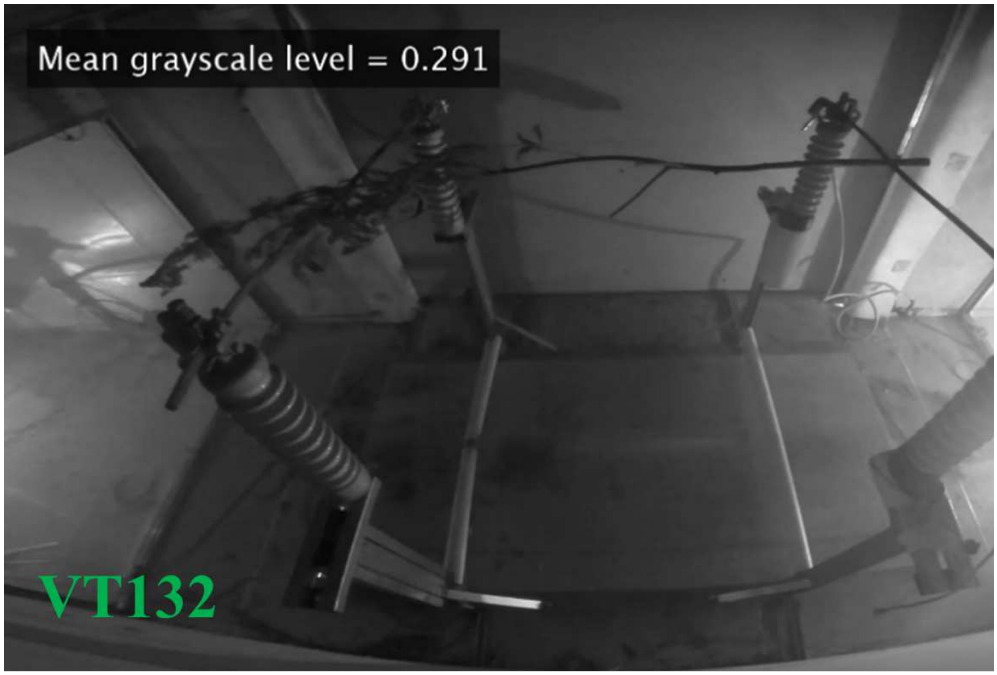


Fig. 3 Pre-energisation baseline reference frame for test VT132 (*A. mearnsii*, 30.3% moisture), captured prior to flame development and used for per-sequence CFI normalisation.



Fig. 4 Flame intensity and fire ignition development during VT132. Captured flame intensity state at 21.13 s into the ph-to-e fault test.

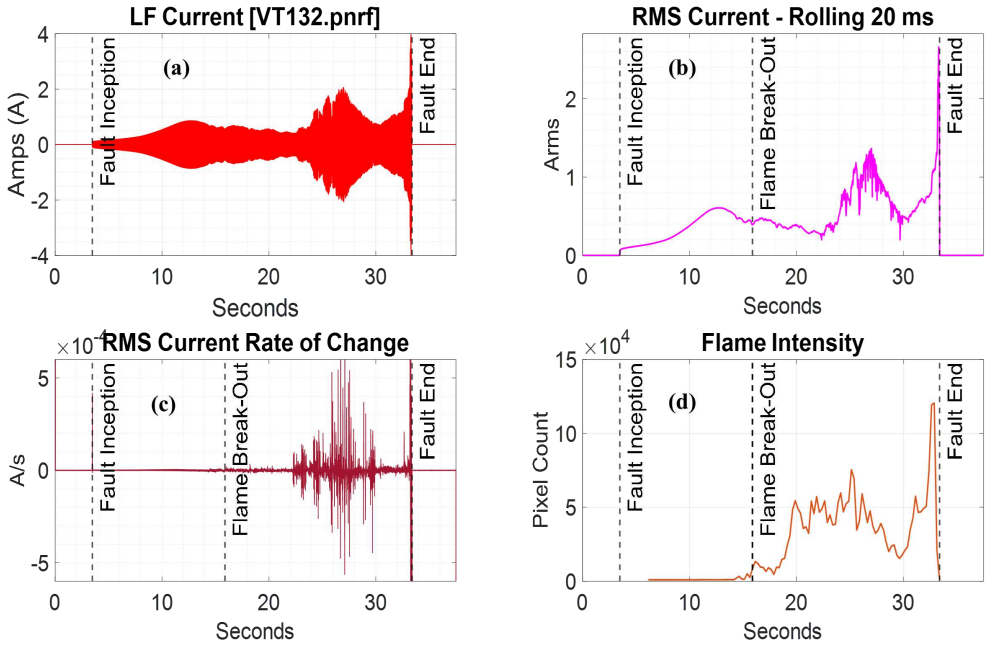


Fig. 5 Concurrent electrical and optical time series for VT132 on the corrected electrical-record time base. (a) LF current at 100 kSa/s; (b) RMS current from a 20 ms rolling window; (c) RMS current rate of change, showing marked volatility from approximately 22 s record time (about 19 s after fault inception); (d) flame intensity as near-white pixel count, showing flame breakout 12.71 s after fault inception.

The time-series data for VT132 comprise the LF current waveform sampled at 100 kSa/s and RMS current values calculated over a 20 ms rolling window. Visual flame breakout is followed by a marked increase in RMS current volatility from approximately 22 s record time (about 19 s after fault inception; Fig. 5c), about 6 s after visual breakout, consistent with progressive charring and intermittent arc re-establishment along the burning branch. Supply was removed when the RMS current reached the 2-A cut-off. The relationship between arc current volatility and the optical signals is examined for a further representative test in Section 5.7. As shown in Fig. 5, the arc energy increases at an approximately steady rate during the pre-breakout charring phase, reflecting progressive resistive heating of the vegetation. Flame breakout occurs at a cumulative arc energy of 52,040 J. The CFI over the full fault duration is 1,925,118 pixel-frames.

The flame intensity metric characterises the spatial and temporal development of combustion at the fault location, but it does not capture airborne ember particles, the primary mechanism of fire spread at distance. The CFI measures the integrated optical output of the combustion event. It does not show whether burning material is ejected, at what rate, or when ejection begins. In addition, its per-sequence normalisation precludes direct cross-test comparison of flame intensity between species or fault configurations. The following section introduces an image-processing pipeline that addresses both limitations: flying-ember detection in HSV

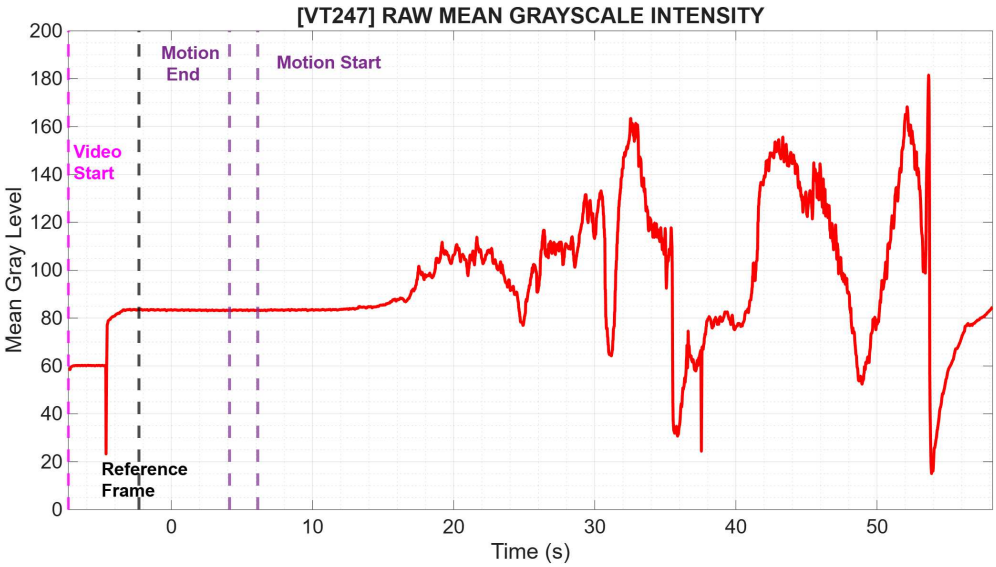


Fig. 6 Raw mean grayscale intensity for VT247.

colour space with plasma-referenced normalisation, which allows cross-test comparison of ember generation.

5 Ember Detection

The original flame intensity analysis quantified combustion using near-white pixel counts (RGB ≥ 0.92) and serves in this study primarily to identify flame breakout and to provide a synchronisation reference. While this metric captured the broad temporal structure of combustion, it was not designed to quantify ember generation and did not distinguish between the electrical arc, sustained flame, and incandescent ember particles ejected from the ignition zone. To address this limitation, a dedicated flying-ember detection pipeline was developed. The algorithm operates in HSV colour space, incorporates frame-to-frame motion differencing to isolate airborne embers from static elements, and applies per-frame exposure normalisation to mitigate automatic camera gain adjustments.

5.1 Reference Frame Normalisation

A key concern with pixel-based intensity analysis is the camera's automatic exposure compensation. The algorithm establishes a reference frame from the pre-energisation period (at $t_0 = -2.21$ s on the corrected electrical-record time base, about 5 s after the video recording started), well before fault inception. For VT247 (Figs. 6–8), the video recording commenced approximately 7.3 s before the current/voltage recording; as stated in Section 3, all times are reported on the corrected electrical-record time base ($t = 0$ s at the start of the current/voltage record).

In Fig. 6, the black dashed line marks the reference frame selected within the stable pre-energisation plateau at ≈83/255. The "Motion Start" and "Motion End" lines delimit the motion baseline window for characterising pre-energisation scene motion. The mean intensity varies from 16 to 181 across the post-energisation period, indicating that uncorrected absolute pixel thresholds produce non-comparable measurements across frames. The deep negative excursions at $t \approx 31$, 36, and 49 s are periods of dense smoke accumulation between the camera and arc, consistent with the negative excursions of the baseline-corrected plasma signal (Fig. 7). All four markers precede energisation, indicating that the reference frame and motion baseline are established under arc-free conditions. Algorithm-derived fire onset and duration were checked against the manual records described in Section 3; tests exceeding the 5% discrepancy threshold without a clear technical explanation were excluded before the statistical analyses reported in Sections 6 and 7. This check validates the timing of combustion events, not the ember pixel counts themselves.

The raw grayscale intensity has stabilised on this plateau (≈83/255) by t_0. The reference frame is validated against two criteria: (i) the mean intensity must fall within a prescribed range on a 0–255 scale, indicating a properly exposed frame that is neither saturated nor underexposed; and (ii) the frame-to-frame motion delta must be below 0.05, indicating a temporally stable scene. For each channel $c \in \{R, G, B\}$, the reference frame's 2nd and 98th percentile intensities are recorded as $P_2^{\text{ref}}(c)$ and $P_{98}^{\text{ref}}(c)$. For every subsequent frame, the percentiles $P_2^{\text{cur}}(c)$ and $P_{98}^{\text{cur}}(c)$ are estimated from a spatially subsampled grid (stride =8, minimum 50,000 pixels) to reduce the computational overhead. Each pixel is mapped from the current frame's dynamic range to the reference frame's dynamic range via:

$$\hat{I}(x, y, c) = p_2^{\text{ref}} + \frac{I(x, y, c) - p_2^{\text{cur}}}{p_{98}^{\text{cur}} - p_2^{\text{cur}}} \left(p_{98}^{\text{ref}} - p_2^{\text{ref}}\right) \tag{1}$$

where $I(x, y, c)$ is the raw pixel value and $\hat{I}(x, y, c)$ is the normalised output, clamped to $[0, 1]$. This normalisation is intended to give identical intensities consistent digital values throughout the recording despite automatic gain adjustments. The percentiles are computed over the whole frame, so a large flame region could shift the mapping; the effect of this was not tested. The normalised image is used for ember HSV classification and motion differentiating. The plasma core detection operates on the raw frame independently.

5.2 Plasma Core Detection

The electrical arc produces an intensely bright near-white region at the fault location. To characterise this plasma core, the raw (unnormalised) frame is converted to grayscale and thresholded at 0.95. All pixels exceeding this threshold are classified as plasma. Plasma detection operates on the raw frame rather than the normalised image used for ember classification. Because the arc plasma core is physically near sensor saturation, its raw brightness reliably exceeds 0.95 regardless of the reference frame's exposure state, ensuring that the plasma count is never suppressed when the reference frame is dim. The normalised image from Equation 1 is reserved exclusively

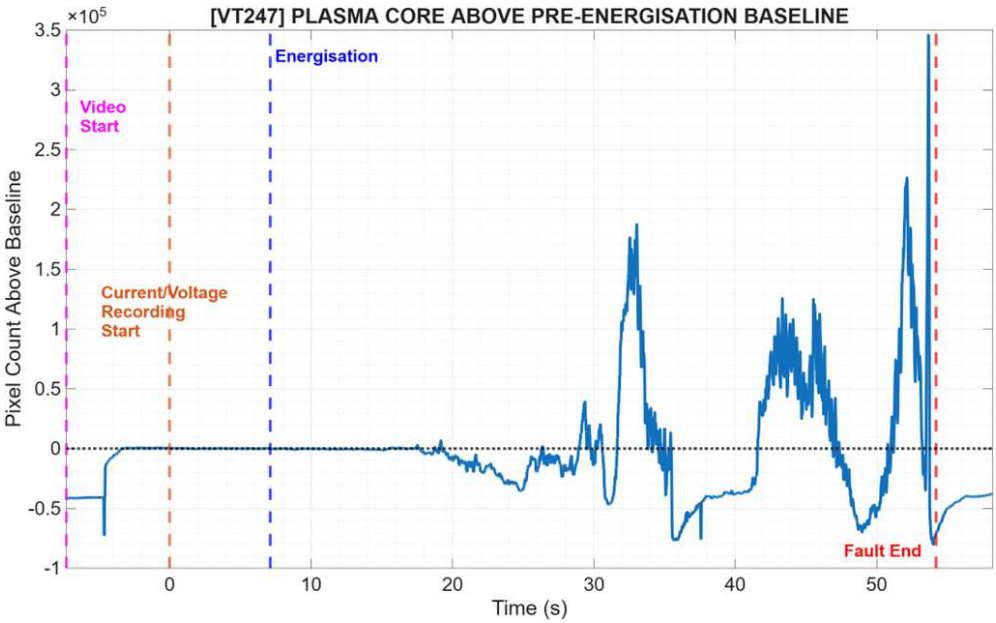


Fig. 7 Sample plasma core result showing corrected plasma core above the pre-energised baseline.

for ember HSV classification and motion differentiating, where exposure-drift correction is essential for stable hue and saturation thresholds. A pre-energisation baseline is established by computing the median plasma pixel count across all frames prior to fault inception, capturing the stable population of near-white pixels produced by ambient test-environment lighting. This baseline is subtracted from the post-energisation plasma series to isolate arc-generated plasma from background illumination:

$$\hat{P}(t) = P(t) - \text{median}\left\{P(\tau) : \tau < t_e\right\} \tag{2}$$

where $P(t)$ is the raw plasma pixel count at time t and t_e is the energisation time.

This baseline-corrected series $\hat{P}(t)$ serves two purposes. Its peak value (specifically, the 95th percentile over the sustained arc-plasma region, excluding any flashover window) provides the normalisation denominator for cross-test flying-ember comparison, placing ember activity on a scale relative to arc intensity under identical camera and lighting conditions. Additionally, the value ceiling $V \leq 0.93$ applied in the ember HSV classifier creates a structural 0.02 gap below the plasma threshold. Because plasma detection operates on the raw frame while ember classification operates on the normalised image, this guard band separates the two classes only approximately: pixels in the arc halo whose normalised value falls below 0.93 may still satisfy the ember colour criteria. Explicit exclusion of the plasma region from the ember mask is a straightforward refinement for future work. For VT247 as shown in Fig. 7, the signal represents the count of near-white pixels (raw grayscale value > 0.95) minus the pre-energisation median, isolating arc-generated plasma from background test-environment lighting. The blue dashed line marks energisation at $t_e = 7.12$ s. The plasma core signal reaches

Table 1 HSV colour thresholds for ember classification.

Parameter	Symbol	Value	Unit / Note
Orange hue range	H_{or}	15°–55°	HSV hue angle
Red hue range	H_{red}	$\leq 15°$ or $\geq 345°$	Wraps at 0°/360°
Min. saturation	$S_{\min}$	0.55	Excludes grey/white
Min. value	$V_{\min}$	0.20	Excludes dark pixels
Max. value	$V_{\max}$	0.93	Guard band below plasma (0.95)

peak intensities of 1.9×10^5 and 3.4×10^5 pixels above baseline at $t \approx 33$ s and $t \approx 53.7$ s, respectively, coinciding with periods of intense arcing; the later peak occurs immediately before fault end. Sustained negative excursions indicate periods of dense smoke accumulation between the camera and the arc, which suppress scene luminance below the pre-energisation level. Apart from the lighting transient at the start of the video recording, the signal is zero throughout the pre-energisation period, consistent with correct baseline subtraction.

5.3 Ember Classification in HSV Colour Space

Rather than relying on a single RGB brightness threshold, the ember detection algorithm operates in the Hue–Saturation–Value (HSV) colour space. This transformation decouples chromatic content from luminance, making classification more robust to variations in illumination, camera exposure, and smoke obscuration. Embers are characterised by their orange-to-deep-red incandescence, mapping to well-defined regions in the HSV cylinder. Table 1 defines the ember colour mask applied to the normalised image.

A pixel is classified as an ember candidate if its hue falls within either the orange band (15°–55°) or the red band ($\leq 15°$ or $\geq 345°$), its saturation exceeds 0.55, and its value lies between 0.20 and 0.93. The upper value bound of 0.93 is set 0.02 below the plasma core threshold of 0.95, preventing any plasma-core pixel from being double-counted as an ember. The minimum saturation of 0.55 excludes desaturated near-white and grey pixels (e.g., smoke) that would otherwise produce false positives in the brightness range. No sensitivity analysis of these HSV thresholds was performed.

Flame regions also fall within these hue and saturation bands. Because flame edges flicker between successive frames at 48 fps, moving flame tips can satisfy both the colour criteria and the motion criterion described below. The flying-ember signal therefore includes some contribution from flame flicker, particularly during vigorous flaming, and is interpreted in this study as an index of optical ember activity rather than a count of individual particles.

5.4 Motion-Based Filtering for Flying Embers

Static red or orange objects in the test rig (e.g., painted surfaces, instrument indicators, or glowing charring on the branch) satisfy the HSV colour criteria but do not represent flying embers. To distinguish airborne incandescent particles from static

scene elements, a frame-to-frame motion differencing algorithm is applied. The absolute difference between the current normalised grayscale frame and the previous frame is computed from:

$$\Delta(x, y, t) = \left| \hat{G}(x, y, t) - \hat{G}(x, y, t-1) \right| \tag{3}$$

where $\hat{G}$ denotes the normalised grayscale image. An adaptive motion threshold is established from a pre-energisation baseline window providing a 2.0 s sample of natural scene motion (e.g., vegetation sway from the test fan). The mean μ_M and standard deviation σ_M of the per-frame average motion magnitude are computed over this window, and the threshold is set as:

$$\theta_M = \max(\mu_M + 3\sigma_M,\ 0.02)\,. \tag{4}$$

The floor of 0.02 prevents the threshold from collapsing to near-zero in calm conditions.

For VT247 as shown in Fig. 8, the baseline window spanned $t = 4$ to 6.2 s, yielding $\mu_M = 0.0023$ and $\sigma_M = 0.0013$; the computed threshold was 0.0062, below the hard floor, so $\theta_M = 0.02$ governed. Between the reference frame and energisation, the flying-ember signal remained negligible (at most 427 pixels, $\hat{E} < 0.01$), well below the 0.05 first-ember threshold; the only larger pre-energisation detections occurred during the lighting transient at the start of the video recording, before the reference frame. Pixels where $\Delta(x, y, t) > \theta_M$ are classified as "moving". The final flying ember mask is the logical intersection of the HSV ember mask and the motion mask, ensuring that only colour-qualified pixels exhibiting inter-frame displacement are counted, effectively filtering out static char, fixed scene elements, and sensor noise. The analysis reported here focuses exclusively on flying (moving) embers. Static ember deposits on surfaces are reserved for a separate study addressing landed-ember accumulation and secondary ignition.

5.5 Morphological Filtering and Plasma-Normalised Ember Activity

After colour and motion classification, the binary ember mask undergoes morphological cleaning. Connected components smaller than 10 pixels are removed using area-opening, eliminating isolated noise pixels. A per-frame ember gate is also applied: if the total ember pixel count in a frame is below 10 pixels, it is set to zero. This two-stage filtering ensures that only spatially coherent ember blobs of physically meaningful size contribute to the reported ember count. To enable cross-test comparison, a normalised ember metric is introduced:

$$\hat{E}(t) = \frac{E(t)}{D}, \quad D = Q_{95}\left\{ \hat{P}(\tau) : \tau \in \mathbb{R} \right\} \tag{5}$$

where E(t) is the flying ember pixel count, Q_{95} is the 95th percentile of the baseline-corrected plasma pixel count over the sustained arc-plasma region (excluding any flashover transient near fault termination), and $\mathbb{R}$ is the sustained arc-plasma region. This dimensionless ratio places ember activity on a scale relative to the arc intensity of the same test, recorded by the same camera, under identical conditions. A value of $\hat{E} =$

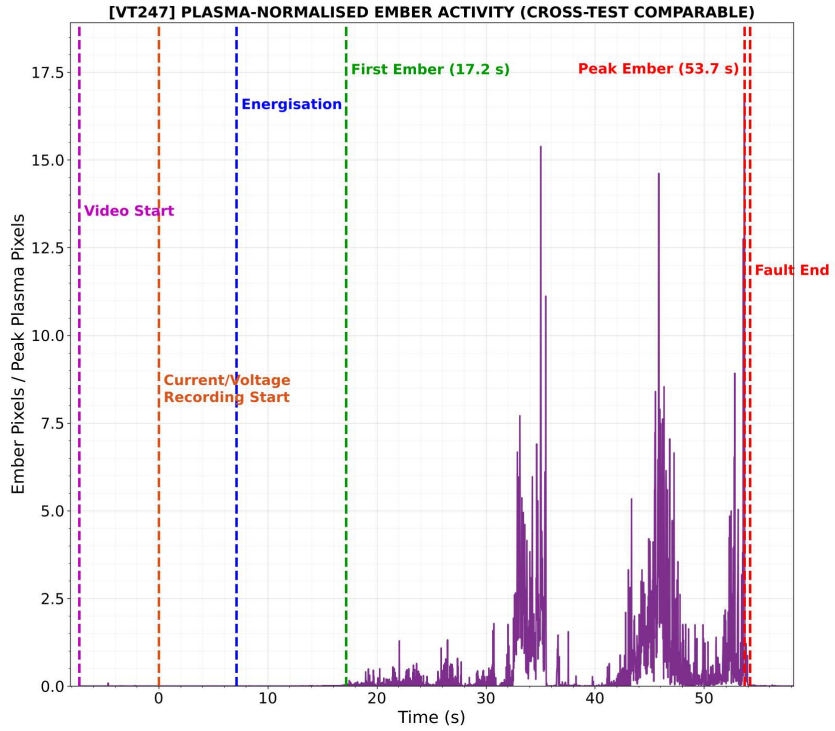


Fig. 8 Plasma-normalised flying ember activity $\hat{E}(t)$ for VT247 (ph-to-e, *P. undulatum*).

1 indicates that the ember pixel area equals the peak plasma area. Values exceeding unity are observed during large burst episodes when substantial firebrand ejection coincides with flame growth, which may partially obscure the arc core and contributes moving flame tips to the ember mask. Values well above unity (for example $\hat{E}_{\text{peak}} = 16.9$ for VT247) may therefore reflect flame contamination of the mask as well as ejection, and should not be read as the area of ember particles. Because both numerator and denominator are derived from the same recording under identical conditions, the ratio is largely insensitive to absolute exposure level. Arc plasma area can, however, vary between tests with arc current, arc geometry, and smoke, so the normalisation supports, rather than guarantees, cross-test comparability.

A flashover transient is flagged when the maximum of $\hat{P}$ in a late-fault candidate window (default: 5 s preceding fault end) exceeds a ratio threshold (default: 5×) relative to the 95th percentile of the preceding sustained region. When flagged, the candidate window is excluded from the denominator computation. This refinement addresses the observation that some phase-to-earth tests terminate with a brief, high-amplitude flashover whose plasma pixel count is several times the sustained arc-plasma level. Retaining such transients would otherwise deflate the normalised ember series for those tests and break cross-test comparability with non-flashover tests. Using a robust percentile over a pre-flashover region yields a denominator representative of sustained arc brightness and preserves comparability across both fault outcomes.

Table 2 Per-test ember statistics extracted by the detection pipeline.

Metric	Symbol	Definition	Units
First ember time	t_{fe}	Time from energisation to first sustained ember frame ($\hat{E} > 0.05$, followed by ≥ 5 frames within 3 s)	s
Peak ember count	e_{peak}	Maximum flying ember pixel count (single frame)	px
Peak ember time	t_{peak}	Time from energisation to peak ember frame	s
Ember duration	D_e	Interval from first ember to fault end (supply removal)	s
Total ember pixels	CEPC	Cumulative pixel-frames over all post-energisation frames	px·frame
Mean ember rate	$\bar{e}$	Mean pixel count during active frames only	px/frame
Burst count	N_b	Number of distinct ejection episodes ($\hat{E} > 1.0$, gap ≥ 1.0 s)	–
Peak normalised FEPC	$\hat{E}_{peak}$	$\max\left(\frac{\text{FEPC}}{95^{\text{th}}\text{-percentile plasma pixel count}}\right)$	–
Total normalised CEPC	$\sum \hat{E}_{\text{norm}}$	$\sum\left(\frac{\text{FEPC}}{95^{\text{th}}\text{-percentile plasma pixel count}}\right)$ over all post-energisation frames	–

5.6 Burst Detection and Temporal Metrics

Ember emission occurs as discrete ejection episodes ("bursts") rather than as a continuous process. A burst is defined as a contiguous run of frames in which the normalised ratio $\hat{E}(t)$ exceeds 1.0, terminated when a gap of at least 1.0 s below this threshold is observed. The $\hat{E} = 1.0$ threshold separates significant ejection activity from low-level background fluctuations, while the 1.0 s gap criterion distinguishes separate episodes from brief inter-frame dips during active ejection at the video frame rate (48 fps). The first ember time is identified as the earliest post-energisation frame at which $\hat{E}(t) > 0.05$, subject to a sustained-activity requirement of at least five additional frames exceeding the same threshold within a 3 s look-ahead window. This two-stage criterion prevents isolated transient detections from being registered as the onset of ember generation. Ember duration is defined as the interval from first ember time to fault end, i.e. supply removal. Because supply was removed when the current reached the pre-set cut-off, D_e reflects both the ember behaviour of the species and the time taken for the fault current to escalate to the cut-off, and it does not include emission after supply removal. The per-test aggregate statistics are summarised in Table 2.

The plasma-normalised ember activity time series $\hat{E}(t)$ for VT247 is shown in Fig. 8, illustrating the discrete burst structure of ember ejection and the near-zero baseline maintained before energisation, indicating few false detections under arc-free conditions in this test. The blue dashed line marks energisation at $t_e = 7.12$ s, with $\hat{E} = 1.0$ marking the level at which ember pixel area equals peak arc plasma area. The first ember detection occurs 10.06 s after energisation (17.18 s on the C/V record time base), preceding the major burst episodes. The burst criterion identifies three distinct ejection episodes at $t = 32.6$–35.5 s, 42.8–47.8 s, and 51.8–53.7 s, with burst maxima of $\hat{E} = 15.4$ ($t = 35.0$ s) and $\hat{E} = 14.6$ ($t = 45.9$ s). The overall peak, $\hat{E}_{\text{peak}} = 16.9$, occurs at $t = 53.7$ s, immediately before fault end, indicating that at maximum ejection intensity the ember mask, which also includes moving flame tips, occupied an area about seventeen times that of the arc plasma core.

5.7 Multimodal Analysis of a Representative Phase-to-Earth Fault

Fig. 9 presents the multimodal time series for VT247 on the common time base. Three temporal phases are identifiable. During the pre-breakout phase, from fault inception ($t = 7.12$ s) to visual flame breakout ($t \approx 19.2$ s), the fault current grows progressively while the flame intensity remains close to its baseline. The first sustained ember detection ($t = 17.18$ s, Fig. 8) precedes visual flame breakout by about 2 s, indicating that low-level ejection of incandescent particles from the charring zone begins shortly before sustained flaming is established; ember activity remains low until the major burst episodes. After breakout, the current envelope becomes increasingly irregular and the RMS current rate of change rises. During the sustained combustion phase ($t \approx 19.2$ to 54.2 s), the three periods of elevated RMS current volatility co-occur with the three flying-ember burst episodes, while in the intervening quiescent periods both the rate of change and the ember signal return close to zero. This co-occurrence is consistent with arc re-ignition events contributing to discrete ember ejection. However, the reverse pathway, in which combustion-generated smoke and char alter the arc (Section 2), cannot be excluded, and the present data establish temporal association rather than causation. The analysis is presented for one representative test; a quantitative event-coincidence analysis across all ph-to-e tests is identified as future work. Vertical dashed lines mark fault inception, flame breakout, first ember, and fault end ($t = 54.2$ s).

6 Fire Occurrence Analysis

Fire occurrence across the 12 tested species was evaluated by examining the binary fire/no-fire outcome against five candidate predictors: initial fault current (A), cut-off current (A), conditioning time (hrs), branch moisture content (%), and branch conductivity (μS/cm). Cut-off current and conditioning time are test settings fixed before each fault, moisture content and conductivity are pre-test fuel properties, and initial fault current is observed at fault inception. The duration of current application (Table 3) was not used as a predictor because it is determined by the time taken for the current to reach the pre-set cut-off, and is therefore a consequence of fault development rather than an independent input. The dataset comprises the 499 valid ph-to-e tests on the twelve species, the fault type considered most representative of real distribution networks; 193 of these tests (38.7%) produced fire. The ember generation analysis presented in Section 7 is further restricted to fire-producing tests. Table 3 summarises the mean values of these parameters per species, aggregated over test groups ranging from 19 (*Schinus molle*) to 59 (*Eu. baxteri*) individual tests. All parameters vary between species.

Cut-off current emerged as the strongest positive predictor of fire outcome across the full dataset, with a point-biserial correlation of $r = 0.44$, substantially exceeding all other tested variables. Because supply was removed when the current reached this pre-set value, a higher cut-off setting allows the fault to progress further into Stage-3 charring before de-energisation, delivering more energy to the branch and possibly increasing the likelihood that burning material falls onto the ground fuel

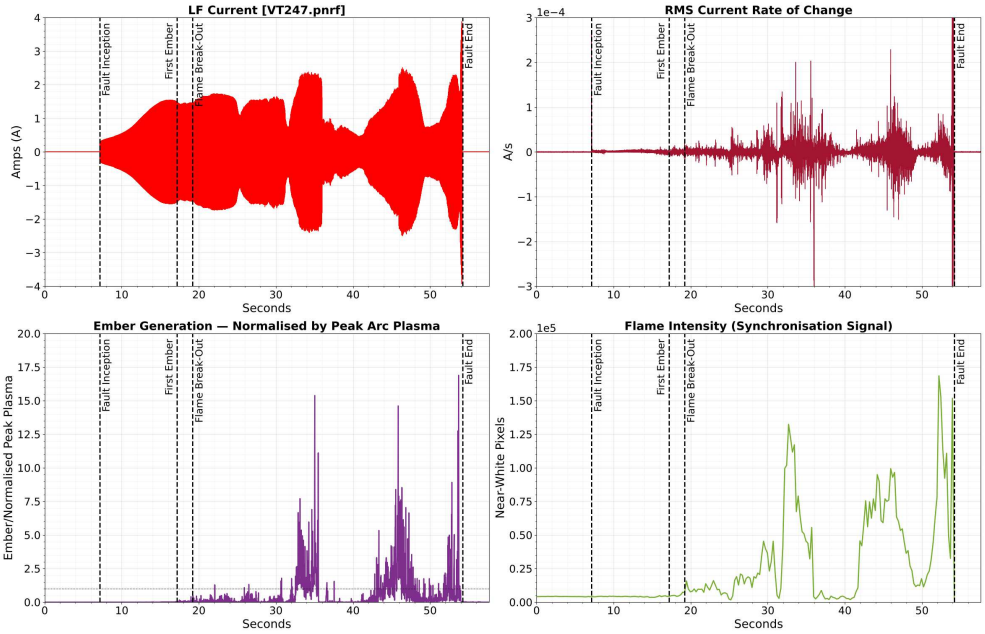


Fig. 9 Four-channel multimodal time series for VT247 on the corrected electrical-record time base. Top left: LF fault current; top right: rate of change of the 20 ms rolling RMS current; bottom left: plasma-normalised flying-ember activity $\hat{E}(t)$; bottom right: flame intensity (near-white pixel count). Vertical dashed lines mark fault inception, flame breakout, first ember, and fault end. Ember burst episodes co-occur with periods of elevated arc current volatility.

Table 3 Summary of mean test parameters and fire outcomes by species for the 499 valid phase-to-earth (12.7 kV) tests.

Species	Group Count	Initial Current (A)	Duration (s)	Cut-off Current (A)	Conditioning Time (hrs)	Moisture (%)	Fire Tests
A. mearnsii	42	0.15	22.2	1.17	10.36	34.38	21
A. melanoxylon	42	0.12	22.7	1.17	22.33	33.24	14
A. pycnantha	29	0.13	21.5	1.14	27.17	31.91	7
A. verticillata	44	0.10	27.1	1.14	14.98	34.49	3
C. glaucophyllus	43	0.16	37.5	1.19	16.02	39.94	14
Eu. baxteri	59	0.15	49.9	1.18	35.36	43.27	30
Eu. viminalis	42	0.17	33.6	1.17	30.86	39.88	19
F. angustifolia	51	0.04	121.5	1.17	14.02	31.15	28
P. undulatum	44	0.23	13.6	1.15	10.78	37.64	6
Pinus radiata	42	0.13	103.7	1.17	14.35	45.47	20
Salix sp.	42	0.08	61.0	1.17	16.27	38.66	31
Schinus molle	19	0.31	3.2	1.18	16.00	53.40	0
All species	499						193

bed. Cut-off setting and exposure time are not separable in this design, so these data cannot show whether the current level itself, or simply the longer energisation it allows, drives the association. The observed fire rate rose from 11.0% at a 0.5 A

Table 4 Fire outcome by pre-set cut-off current for the 499 phase-to-earth tests.

Cut-off (A)	Tests	Fire	No fire	Fire rate (%)
0.5	164	18	146	11.0
1.0	171	69	102	40.4
2.0	164	106	58	64.6
All	499	193	306	38.7

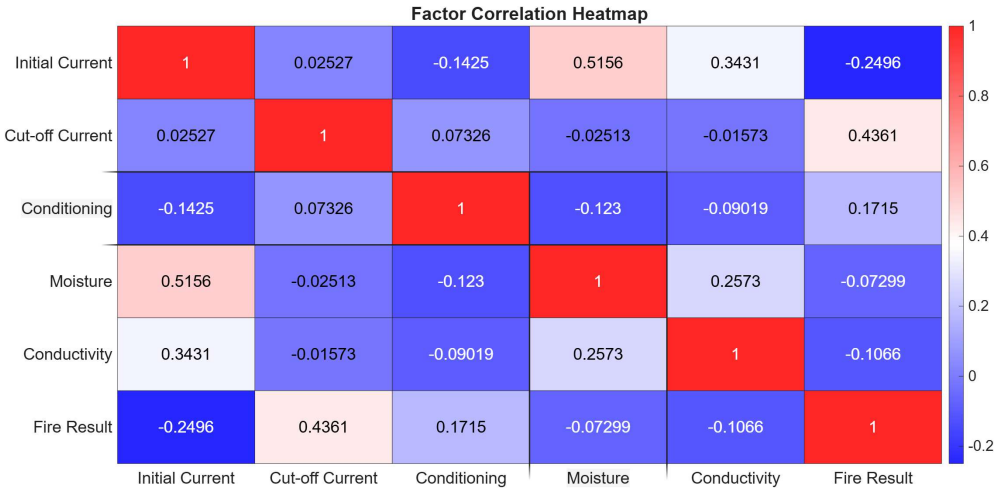


Fig. 10 Pairwise correlation structure across the five candidate predictors and the binary fire outcome, computed on the 396 tests with complete data for all five predictors.

cut-off to 40.4% at 1 A and 64.6% at 2 A (Table 4). Median fault duration in no-fire tests also lengthened with the cut-off setting (8.6, 12.3, and 29.2 s), whereas fire-producing tests ran for a median of 63–73 s at all three settings. Initial fault current showed a negative association ($r = -0.25$), indicating that tests initiated at lower arc current amplitudes were more likely to result in fire. This is consistent with the fault physics described in Section 2: branches that establish low-current, high-impedance contacts take longer to reach the cut-off current, so progressive charring can develop into sustained combustion before supply is removed. Conditioning time exhibited a weaker positive correlation ($r = 0.17$), consistent with the expectation that extended pre-fault conditioning reduces branch moisture and lowers the energy threshold for sustained ignition. Moisture content ($r = -0.07$) and branch conductivity ($r = -0.11$) showed negligible marginal associations with fire outcome.

Fig. 10 illustrates the pairwise correlation structure across the five candidate predictors and the binary fire outcome, computed on the 396 tests with complete data for all five predictors. Most predictor pairs are weakly correlated ($|r| < 0.35$); the exception is moisture content and initial fault current ($r = 0.52$). This moderate correlation does not preclude joint inclusion in the multiple logistic regression model but

must be considered when interpreting the adjusted moisture coefficient. The dominance of cut-off current was consistent across all eleven species that produced fire, with species-level point-biserial correlation scores ranging from 0.24 (*F. angustifolia*) to 0.73 (*A. mearnsii*). The substantially higher correlation for *A. mearnsii* indicates that fire-producing tests in this species are tightly coupled to arc current escalation, with fire outcomes reliably associated with higher cut-off currents. *F. angustifolia*, by contrast, exhibits a much weaker current-threshold relationship, which fits its low mean initial current (0.04 A) and long mean fault duration (Table 3). Fire outcomes in *F. angustifolia* appear to depend more on prolonged low-current arc exposure than on a discrete current escalation event, which may matter for protection relay calibration.

Multiple logistic regression was fitted with cut-off current (I_{co}), initial fault current (I_0), and branch moisture content (θ) as predictors, using the 496 tests with complete data for these variables (Table 5). Expressed in standardised predictors (z-scores of I_{co}, I_0, and θ), the fitted model is:

$$\log\left(\frac{p}{1-p}\right) = -0.65 + 1.08\, z_{\mathrm{co}} - 1.06\, z_0 + 0.22\, z_\theta, \tag{6}$$

where p is the probability of a fire-producing outcome. The model improves substantially on the intercept-only model (likelihood-ratio $\chi^2(3) = 150.3$, $p = 2.3 \times 10^{-32}$; residual deviance 511.8; McFadden pseudo-$R^2 = 0.23$) and discriminates fire from no-fire outcomes in-sample (area under the ROC curve 0.82; no cross-validation was performed), although the Hosmer–Lemeshow test indicates imperfect calibration ($p = 0.001$). Variance inflation factors do not exceed 1.43. Cut-off current and initial fault current are both highly significant ($p < 10^{-8}$), whereas moisture content is not ($p = 0.10$). Each 1 A increase in the cut-off setting multiplies the odds of fire by 5.65 (95% CI 3.92–8.14), and each 0.1 A increase in initial current multiplies them by 0.38 (95% CI 0.27–0.52). The opposing signs on cut-off and initial current are consistent with the physical sequence of fault development: ignition is favoured when a fault commences at low arc current and subsequently escalates to a high cut-off current, reflecting progressive carbonisation associated with Stage-3 charring. Moisture content has a small, non-significant positive coefficient despite a weak negative marginal association with fire ($r = -0.07$). Because moisture content is positively correlated with initial fault current ($r = 0.52$), which enters the model with a negative coefficient, this sign reversal is consistent with statistical suppression rather than a physical effect; when species is accounted for, the moisture coefficient becomes negative and remains non-significant (Table 5). Moisture content was therefore not a significant predictor of fire occurrence in this dataset. Moisture was measured on an end-cut sample rather than at the contact point, so measurement error may have attenuated its apparent effect.

Fig. 11 presents the observed fire probability, the proportion of fire-producing tests, for each of the 12 species. Fire probability ranges from 73.8% for *Salix* sp. to 6.8% for *A. verticillata* and zero for *Schinus molle*. Because the cut-off settings were balanced within each species (mean cut-off 1.14–1.19 A; Table 3), these differences are not explained by the cut-off setting, and the two-current model does not fully capture them: evaluated at species-mean predictor values, it predicts fire probabilities of 0.48

Table 5 Logistic regression of fire outcome and sensitivity analyses for within-species dependence. Coefficients (β) are on the log-odds scale with standard errors in parentheses. The species fixed-effects (FE) model excludes *Schinus molle*, which produced no fires; GEE uses an exchangeable working correlation within species; cluster-robust standard errors are grouped by species (12 clusters).

Term	Main model ($n = 496$) β (SE)	p	OR (95% CI)	Species FE ($n = 477$) β (SE), p	GEE ($n = 496$) β (SE), p	Cl.-robust p
Intercept	−2.51 (0.68)	< 0.001	–	–	−0.51 (0.87), 0.56	0.023
Cut-off (per A)	1.73 (0.19)	< 0.001	5.65 (3.92–8.14)	2.16 (0.23), < 0.001	1.62 (0.28), < 0.001	< 0.001
Initial (per 0.1 A)	−0.97 (0.16)	< 0.001	0.38 (0.27–0.52)	−0.72 (0.19), < 0.001	−0.62 (0.16), < 0.001	< 0.001
Moisture (per %)	0.031 (0.019)	0.10	1.03 (0.99–1.07)	−0.038 (0.031), 0.22	−0.020 (0.023), 0.38	0.28

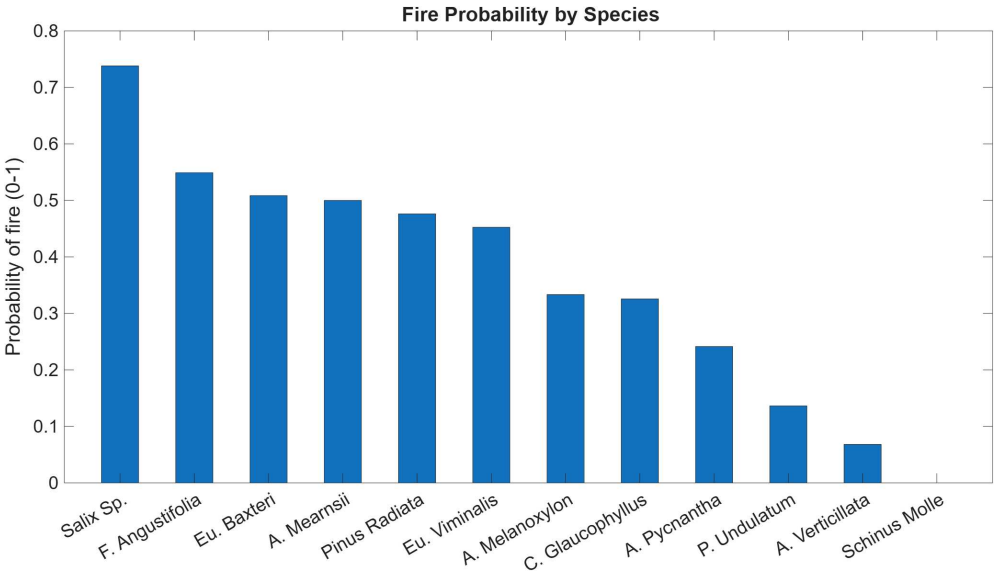


Fig. 11 Observed fire probability (proportion of fire-producing tests) by species for the 499 phase-to-earth tests.

for *Salix* sp., 0.40 for *A. verticillata*, and 0.15 for *Schinus molle*. Species identity therefore carries information about fire susceptibility beyond the initial and cut-off currents, a heterogeneity masked in the whole-dataset analysis. A mixed-effects model with species random intercepts and cut-off-by-species interactions would address this and was not fitted here.

Species-level correlations between each factor and fire outcome (Fig. 12) show that cut-off current is positively associated with fire in every species that produced fire ($r = 0.24$–0.73). Initial fault current is negatively associated with fire in all species except *Salix* sp. ($r = 0.10$) and *Pinus radiata* ($r \approx 0$). Within species, moisture content is negatively associated with fire in nine of the eleven species shown (e.g. $r = -0.34$ for *Eu. baxteri* and $r = -0.35$ for *A. melanoxylon*), consistent with the conventional role of moisture in impeding ignition and with the interpretation of the positive pooled coefficient as a suppression effect. The relative strength of each association varies between species, which may matter for tuning fault detection to the dominant vegetation type in a given powerline corridor.

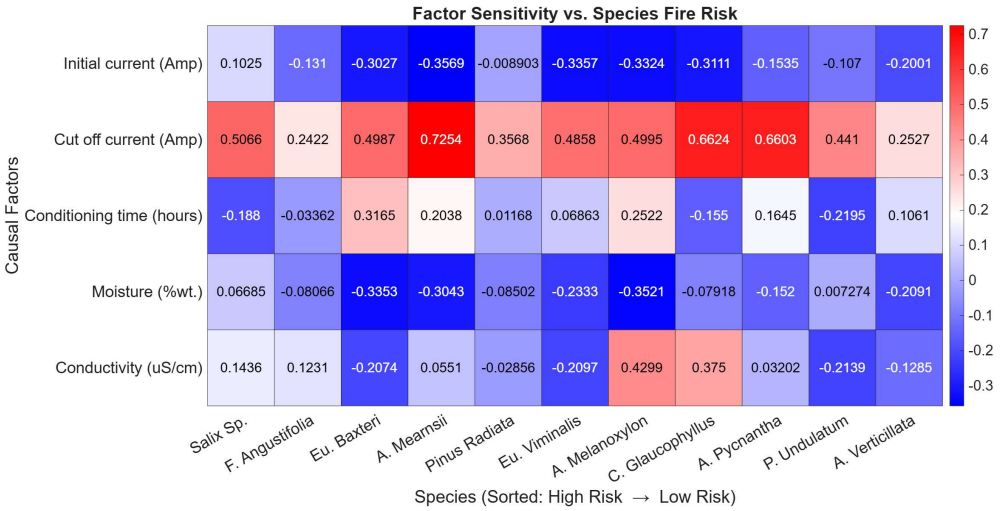


Fig. 12 Species-level point-biserial correlations between each candidate factor and the fire outcome. Species are ordered from highest to lowest observed fire rate; *Schinus molle* is not shown because it produced no fire-producing tests.

The logistic regression model in Equation 6 treats individual tests as independent observations, whereas multiple tests were conducted on branches of the same species and residual within-species correlation is likely. To test the sensitivity of the conclusions to this dependence, the model was refitted with species fixed effects, with generalised estimating equations (GEE) using an exchangeable working correlation within species, and with cluster-robust standard errors grouped by species (Table 5). The cut-off and initial current effects remained highly significant in all three analyses ($p < 0.001$), with cut-off coefficients of 2.16 (fixed effects) and 1.62 (GEE) per ampere and initial current coefficients of -0.72 and -0.62 per 0.1 A. The moisture coefficient became negative (-0.038 and -0.020) and remained non-significant ($p = 0.22$ and 0.38). The principal fire-occurrence findings are therefore robust to within-species dependence, although with only twelve species clusters the GEE and cluster-robust standard errors should be regarded as approximate.

7 Ember Generation

The ember analysis covers 132 of the 193 fire-producing ph-to-e tests, from ten species (Table 6). Because ember generation was characterised only for fire-producing tests, the ember metrics describe the behaviour of faults that ignited the ground fuel bed and cannot be used to discriminate fire from no-fire outcomes.

Species effects on each ember metric were tested by one-way ANOVA and by generalised linear models (GLMs) with a Gaussian (normal) family and identity link, with species as a categorical predictor and *A. mearnsii* as the reference level; GLM coefficients are therefore differences in species means relative to *A. mearnsii*, in the units of the metric. Moisture content, initial fault current, and branch diameter were examined as additional continuous predictors in the same GLM framework.

7.1 Total Ember Quantity

No statistically significant inter-species difference in total normalised ember quantity was detected (one-way ANOVA, $p = 0.90$). When combustion is established and ember generation begins, the integrated volume of ember material produced over the full fault duration is broadly comparable across species when normalised by arc plasma intensity. This contrasts with the highly significant species effects on the temporal and intensity metrics below, and suggests that species identity is associated with *when* and *at what intensity* embers are produced rather than with how much ember material is generated in aggregate.

Neither initial fault current (Spearman $r = -0.007$, $p = 0.94$) nor branch diameter (Spearman $r = -0.21$, $p = 0.07$) reached statistical significance as predictors of total ember quantity. Moisture content was the only continuous variable to show a statistically significant positive effect on total ember quantity (univariate GLM: $\beta = 5{,}935$, $p = 0.008$; species-controlled GLM: $\beta = 9{,}825$, $p = 0.003$). Higher branch moisture was associated with greater total ember quantity, a counter-intuitive finding given moisture's conventional role in suppressing combustion. One candidate explanation is a conductivity hypothesis: branches with higher moisture may be more conductive in the early fault stages, sustaining the arc at higher current and extending the fault before the cut-off is reached. The test records support the first part of this hypothesis but not the second. Moisture content is positively correlated with initial fault current (Spearman $\rho = 0.58$, $p < 10^{-44}$, $n = 496$), but it is negatively correlated with fault duration across all tests ($\rho = -0.27$, $p < 10^{-9}$) and unrelated to fault duration among fire-producing tests ($\rho = 0.07$, $p = 0.33$, $n = 192$). Wetter branches therefore reach the cut-off current sooner rather than later, and prolonged energy delivery does not explain the moisture–ember association. Alternative explanations, including moisture-dependent differences in pyrolysis rate, char porosity, and steam-assisted particle ejection, remain possible. This relationship should therefore be treated as a hypothesis requiring dedicated experimental investigation, including direct measurement of arc impedance evolution as a function of branch moisture content across species. Because the association was observed under laboratory conditioning at a single simulated fire-weather condition, it should not be extrapolated to seasonal field conditions without dedicated outdoor investigation.

7.2 Time to First Ember

Species identity was the strongest statistical determinant of time to first ember (ANOVA $p = 2.99 \times 10^{-12}$, GLM pseudo-$R^2 = 0.44$). Mean times to first ember spanned a sevenfold range, from 9.1 s for *P. undulatum* to 66.0 s for *F. angustifolia*. *P. undulatum* (9.1 s) and *Eu. viminalis* (11.9 s) exhibited the shortest mean onset times, both producing detectable embers within 12 s of energisation on average, although the *P. undulatum* sample is small ($n = 4$). The majority of species including *Eu. baxteri* (13.3 s), *A. mearnsii* (14.9 s), *Salix* sp. (16.1 s), *C. glaucophyllus* (16.1 s), *A. pycnantha* (16.8 s), and *A. melanoxylon* (18.5 s) clustered within a 13–19 s range.

Two species were identified as significant statistical outliers. *Pinus radiata* showed a mean onset time of 51.4 s (GLM estimate: 36.5 s above the *A. mearnsii* baseline;

$p < 0.001$), and *F. angustifolia* showed 66.0 s (51.1 s above baseline; $p < 0.001$). *Pinus radiata* has the highest mean moisture content of the species in the ember analysis (45.5%), pointing to a prolonged moisture-expulsion phase, whereas *F. angustifolia* has the lowest (31.2%) but also by far the lowest mean initial fault current (0.04 A), so its delay is more plausibly related to slow current growth through a high-impedance contact. For protection systems calibrated to rapid-ignition signatures, this extended pre-ember window is a risk interval that fixed-duration fault timers may underestimate. Tests in which no ember was detected do not contribute an onset time; a survival-analysis treatment of these right-censored observations would be a useful extension.

7.3 Ember Duration

Ember duration varied significantly across species (ANOVA $p = 9.5 \times 10^{-9}$, GLM pseudo-$R^2 = 0.36$). *Pinus radiata* exhibited the longest mean emission duration of 97.1 s, approximately four times that of *A. mearnsii* (24.7 s), and was statistically distinguishable from all other species at $p < 0.001$. *C. glaucophyllus* (72.6 s), *F. angustifolia* (56.1 s), and *Eu. baxteri* (55.7 s) each showed significantly elevated durations relative to baseline ($p < 0.001$). *Pinus radiata* combines delayed onset with prolonged duration: slow ignition followed by the longest sustained ember window of any tested species. Once ember generation begins, *Pinus radiata* continues to emit embers for approximately 100 s on average before supply is removed. Because ember duration ends at supply removal, this long window also reflects the slow escalation of fault current towards the pre-set cut-off in this species (Table 3). This extended hazard window matters most when protection operates late or recloser cycling lets the fault persist beyond standard trip timeouts, so that the effective ember generation interval far exceeds that of fast-igniting species. This "slow fuse, long burn" profile may be underweighted in current probabilistic wildfire risk models that use ignition onset time as the primary species parameter.

7.4 Peak Ember Count

Species identity had a statistically significant effect on peak single-frame flying ember pixel count (ANOVA $p = 1.1 \times 10^{-4}$, GLM pseudo-$R^2 = 0.24$). *Salix* sp. produced the highest mean peak ember count (1,325,913 px), representing a 2.6-fold elevation above the *A. mearnsii* baseline ($p < 0.001$). *F. angustifolia* (909,019 px, $p < 0.05$) and *Eu. baxteri* (900,679 px, $p < 0.05$) also showed significantly elevated peak counts. Peak normalised ember rate showed no significant species effect (ANOVA $p = 0.42$), suggesting that the absolute intensity of burst episodes is governed primarily by test-specific arc energy trajectory rather than species identity.

7.5 Combined Predictors and Species Risk Profiles

Considering the three ember metrics that differ significantly between species (time to first ember, ember duration, and peak ember count), three provisional risk profiles are proposed. These profiles are assigned qualitatively from the species means in Table 6; a formal clustering on standardised metrics with larger samples is required to confirm

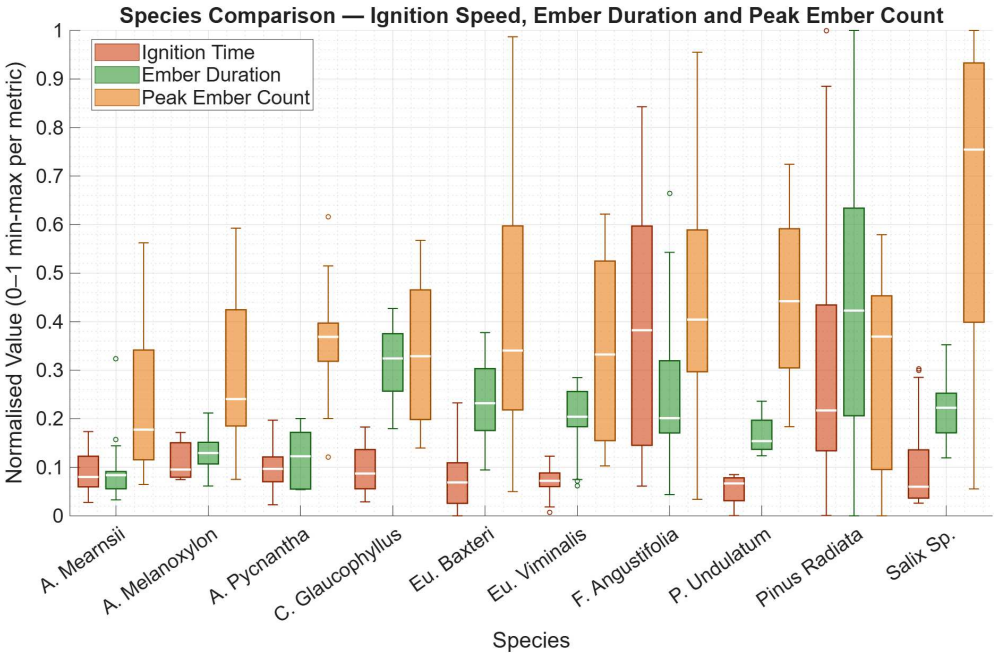


Fig. 13 Cross-species distributions of time to first ember (ignition time), ember duration, and peak ember count, each min–max normalised across all tests.

them. Several species means rest on four to eight tests, no correction for multiple comparisons was applied, and time to first ember and ember duration are both bounded by the time the current takes to reach the cut-off, so part of the between-species difference may reflect the termination rule rather than the species. First, *Eu. baxteri* and *Eu. viminalis* represent a *fast-igniting* profile: both species produce embers within 12–13 s of energisation and sustain generation for 48–56 s. They also have the largest mean total ember quantities, although total quantity did not differ significantly between species. These species merit further study for network vegetation management. Second, *Salix* sp. constitutes a *burst-dominant* profile, defined by the highest peak single-frame ember count of all tested species. With an ignition onset time (16.1 s) comparable to the main species cluster, *Salix* sp. produces discrete, high-intensity ejection episodes, which may favour the simultaneous release of many particles; whether this increases long-distance transport depends on ember size and mass, which were not measured. Third, *Pinus radiata* and *F. angustifolia* represent a *delayed-sustained* profile: prolonged time to first ember (51–66 s) combined with the longest emission durations (97 s and 56 s, respectively) gives a risk profile that is offset in time from the fast-igniting species but not necessarily lower in consequence.

Fig. 13 compares the distributions of the three species-discriminating ember metrics. *Eu. baxteri* and *Eu. viminalis* show short, tightly distributed ignition times. *Salix* sp. has the highest median peak ember count. *Pinus radiata* and *F. angustifolia* show the widest spread in ignition time, and *Pinus radiata* the longest ember durations.

Table 6 Provisional species profile of optical ember metrics during phase-to-earth electrical faults; risk labels are qualitative and not validated. Rows are ordered by mean total ember quantity for presentation only; this metric did not differ significantly between species (ANOVA $p = 0.90$).

Species	N	Total Ember Qty (norm. px)	Ember Duration (s)	Peak Ember Count (px)	Peak Ember Rate (norm.)	Time to 1st Ember (s)	Risk profile
Eu. baxteri	22	93,245	55.7	900,679	1,836	13.3	High Fast ignition
Eu. viminalis	15	61,922	47.9	744,096	2,477	11.9	High Fast ignition
Salix sp.	23	12,333	52.5	1,325,913	413	16.1	High Intense peak bursts
A. pycnantha	6	26,559	30.5	774,300	316	16.8	Moderate Balanced risk
F. angustifolia	20	26,448	56.1	909,019	708	66.0	Moderate Long duration, high peak
C. glaucophyllus	8	16,991	72.6	718,851	278	16.1	Moderate Balanced risk
Pinus radiata	12	12,856	97.1	646,261	283	51.4	Moderate-high Longest duration
P. undulatum	4	8,051	40.4	937,513	129	9.1	Low-moderate Moderate peak
A. mearnsii	16	4,712	24.7	505,616	143	14.9	Low Shortest duration
A. melanoxylon	6	2,832	32.8	633,652	67	18.5	Low Short duration
ANOVA p-value		0.90 (ns)	9.5×10^{-9}	1.1×10^{-4}	0.42 (ns)	3.0×10^{-12}	

A per-species ember generation risk profile for the ten species with sufficient comparative test results is presented in Table 6. *A. verticillata* and *Schinus molle* are excluded: *Schinus molle* produced no fire-producing ph-to-e tests, and *A. verticillata* produced only three (Table 3), none of which was retained in the ember dataset. Three of the five metrics show highly significant species effects: time to first ember ($p = 3.0 \times 10^{-12}$), ember duration ($p = 9.5 \times 10^{-9}$), and peak ember count ($p = 1.1\times10^{-4}$). Total ember quantity ($p = 0.90$) and peak ember rate ($p = 0.42$) show no significant species differentiation. The risk profile in the rightmost column summarises these multi-metric assessments as provisional risk tiers. Among all the tested species, *Eu. baxteri* has the highest mean total ember quantity (93,245 normalised pixel-frames, although this metric does not differ significantly between species) with a fast-ignition profile (mean time to first ember 13.3 s). *Salix* sp. leads all species in peak ember count (1,325,913 px), consistent with its burst-dominant risk character despite a moderate total quantity. *Pinus radiata* records the longest ember duration (97.1 s), approximately four times that of the reference species *A. mearnsii* (24.7 s), underscoring its sustained-emission risk profile.

Fig. 14 shows the ember risk profiles of the six species with the highest composite scores: *Eu. baxteri* (0.71), *Eu. viminalis* (0.64), *Salix* sp. (0.50), *C. glaucophyllus* (0.41), *P. undulatum* (0.37), and *A. pycnantha* (0.33). *Eu. baxteri* and *Eu. viminalis* display broad profiles combining high ignition speed with the largest total ember quantity and peak ember rate, respectively. *Salix* sp. exhibits a distinctively asymmetric profile concentrated on the peak ember count axis, reflecting its burst-dominant ejection character. *C. glaucophyllus* is weighted towards ember duration, whereas *P. undulatum* and *A. pycnantha* score mainly on ignition speed. The delayed-sustained species fall just outside the six highest scores (*Pinus radiata* 0.33, *F. angustifolia*

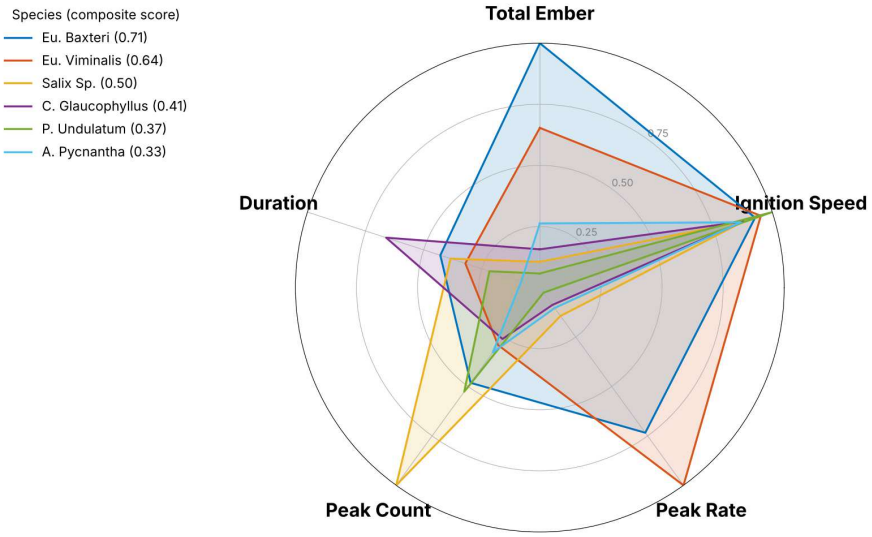


Fig. 14 Ember risk profiles for the six species with the highest composite ember score, in radar chart form. Each axis represents one of the five normalised ember metrics. The axes are scaled between 0 and 1 across all tested species, and the time-to-first-ember axis is inverted so that radially outward positions correspond to higher risk on all five dimensions. Values are the species means in Table 6; the composite score shown in the legend is the mean of the five normalised metrics.

0.29), because their long ember durations are offset by slow ignition. This visualisation provides a compact, multi-dimensional summary of species-level ember risk that complements the univariate analyses in the preceding subsections. It is a descriptive summary of optical ember metrics, not a validated risk ranking.

8 Conclusions

This study presented a multimodal analysis of vegetation ignition dynamics under high-impedance fault (HIF) conditions, using 499 staged fault tests on twelve species (seven native Australian and five introduced) from the Victorian Vegetation Conduction Ignition Testing programme. All tests were phase-to-earth faults at 12.7 kV. Fire occurrence was analysed by binary logistic regression, and ember generation was analysed for the fire-producing tests using an HSV colour-space ember detection pipeline, with a Cumulative Flame Intensity (CFI) signal used to identify flame breakout.

Among the predictors tested, the pre-set cut-off current was the strongest positive predictor of fire (point-biserial $r = 0.44$; standardised coefficient 1.08; odds ratio 5.65 per ampere), and initial fault current was negatively associated with fire ($r = -0.25$; standardised coefficient -1.06). Because supply was removed when the current reached the cut-off, cut-off setting and exposure time cannot be separated in this design. The pairing is consistent with fire being favoured when a fault begins at low current and is allowed to escalate through Stage-3 charring before de-energisation, but the data do

not show whether the current level or the longer energisation it permits is responsible. Raising the cut-off setting from 0.5 to 2 A was associated with an increase in the observed fire rate from 11% to 65%, and both current effects remained significant in the species fixed-effects, GEE, and cluster-robust analyses. Moisture content was not a significant predictor of fire, although it was measured on an end-cut sample and not at the contact point. The HSV-based pipeline gave significant inter-species differences in time to first ember, ember duration, and peak single-frame ember pixel count, whereas total ember quantity did not differ between species. These differences are partly bounded by the termination rule, rest on small samples for several species, and were not corrected for multiple comparisons. Three provisional groupings of optical ember behaviour were described: fast-igniting (*Eu. baxteri* and *Eu. viminalis*), burst-dominant (*Salix* sp.), and delayed-sustained (*Pinus radiata* and *F. angustifolia*). In one representative test (VT247), ember burst episodes co-occurred with periods of elevated arc current volatility; this is a temporal association in a single test, not evidence of a general or causal link.

The findings are best treated as hypothesis-generating for three areas. For network protection engineering, the cut-off current in these tests is analogous to a protection pickup threshold, and the association is consistent with lower-current de-energisation being linked to fewer ground-fuel ignitions in this laboratory configuration. It does not show that lowering relay pickup settings would reduce ignitions in the field. That would require testing under time–current protection characteristics, current-limiting systems, and field conditions. For vegetation management, the species differences in optical ember metrics identify species for further study, but with the present sample sizes and the termination-rule confound they do not support clearance priorities. For wildfire risk modelling, the onset-time, duration, and peak-burst metrics are laboratory-derived optical quantities. They are not firebrand source terms, because particle size, mass, temperature, and transport were not measured.

Several limitations bound the scope of these conclusions. All experiments were conducted in a controlled indoor laboratory at a single simulated fire-weather condition, without ambient wind, humidity gradients, or solar radiation, and only phase-to-earth faults were analysed. The fire/no-fire outcome and its criteria come from the original test programme. The logistic model treats cut-off and exposure time as inseparable, was assessed in-sample (area under the ROC curve 0.82) without cross-validation, showed imperfect calibration (Hosmer–Lemeshow $p = 0.001$), and under-predicted species with high fire rates. Within-species dependence was examined by fixed-effects, GEE, and cluster-robust analyses, but with only twelve species clusters these estimates are approximate, and a mixed-effects model was not fitted. Moisture content was measured on an end-cut sample, and the positive moisture–ember association remains mechanistically unexplained; the test records do not support the hypothesis that wetter branches prolong the fault. The ember pipeline was not validated against particle-level ground truth. Moving flame tips can contribute to the flying-ember mask, the separation between arc plasma and ember pixels is approximate, and neither the exposure normalisation nor the HSV thresholds were tested for sensitivity. The ember metrics are therefore best interpreted as an optical activity index. Ember duration and time to first ember depend on the time the current takes to reach the cut-off.

Ember metrics were computed only for 132 of the 193 fire-producing tests, so they cannot discriminate fire from no-fire outcomes, and the excluded tests may differ systematically. Species comparisons were made without multiple-comparison correction, several species have four to eight tests, and the risk profiles are qualitative. The arc-current and ember coupling was examined in one test. The pipeline was developed on 48 fps laboratory video, and its performance under different illumination, frame rates, or outdoor arc morphologies has not been characterised.

Future investigations should extend the experimental programme to outdoor conditions incorporating wind exposure, varied ambient humidity, and multi-conductor fault geometries representative of real distribution network configurations. Manual annotation of ember particles on a stratified sample of frames, together with particle tracking to separate ballistic embers from flame flicker, would quantify the precision and recall of the detector. Extending ember characterisation to no-fire tests, so that the ember metrics can be related to the fire outcome, and testing the coincidence of ember bursts with arc volatility across all phase-to-earth tests against a randomised null, would strengthen the mechanistic interpretation. Measurement of arc impedance as a function of branch moisture content throughout the fault duration would provide a direct test of the conductivity hypothesis and clarify the causal pathway from moisture to ember generation. Application of mixed-effects logistic regression with larger within-species sample sizes would strengthen species-level inference and support the development of species-specific relay calibration recommendations. Integration of the species risk indices into geospatial firebrand transport and fire propagation models is a near-term priority for translating the laboratory findings into actionable network asset management tools.

Acknowledgements. The authors thank the Victorian Government and Marxsen Consulting Pty Ltd for making the Vegetation Conduction Ignition Testing data and video recordings publicly available.

Declarations

Funding. No funding was received for conducting this study.

Competing interests. The authors have no competing interests to declare that are relevant to the content of this article.

Ethics approval and consent. Not applicable. This study is a secondary analysis of publicly available laboratory test data and involved no human participants or animals.

Author contributions. R. Li: Conceptualisation, Methodology, Investigation, Formal Analysis, Writing – Original Draft.
C. Ozansoy: Supervision, Conceptualisation, Writing – Draft, Review and Editing.

Data availability. The underlying test data and video recordings are publicly available from the Victorian Government Victorian Government (2016).

Code availability. The MATLAB analysis code is available from the corresponding author upon reasonable request.

References

Ashok V, Yadav A (2021) Fault diagnosis scheme for cross-country faults in dual-circuit line with emphasis on high-impedance fault syndrome. IEEE Systems Journal 15(2):2087–2097. https://doi.org/10.1109/JSYST.2020.2991770

Bilancia LF (2020) Electrical fire patterns in vegetation. In: 2020 IEEE Symposium on Product Compliance Engineering (SPCE Portland), pp 1–6, https://doi.org/10.1109/SPCE50045.2020.9296155

Cong Z, et al (2023) Study on the mechanism and electrical characterization of the tree-contact incipient fault in the non-effectively grounded system. IEEE Transactions on Power Delivery 38(3):1709–1719. https://doi.org/10.1109/TPWRD.2022.3221481

Earth Science Technology Office (2020) Wildfire risk and power lines. NASA. https://esto.nasa.gov/firetech/wildfire-risk-and-powerlines/

Finney MA, et al (2015) Role of buoyant flame dynamics in wildfire spread. Proceedings of the National Academy of Sciences 112(32):9833–9838. https://doi.org/10.1073/pnas.1504498112

Gao W, He WX, Wai RJ, et al (2024) High-impedance arc fault modeling for distribution networks based on dynamic geometry dimension. Electric Power Systems Research 229:110109. https://doi.org/10.1016/j.epsr.2023.110109

Gomes DPS, Ozansoy C, Ulhaq A (2020) Vegetation high-impedance faults' high-frequency signatures via sparse coding. IEEE Transactions on Instrumentation and Measurement 69(7):5233–5242. https://doi.org/10.1109/TIM.2019.2950822

Hadden RM, Scott S, Lautenberger C, et al (2011) Ignition of combustible fuel beds by hot particles: an experimental and theoretical study. Fire Technology 47:341–355

Hu Y, Ye X, Liu Y, et al (2023) FireFly: A synthetic dataset for ember detection in wildfire. In: Proceedings of the IEEE/CVF International Conference on Computer Vision Workshops (ICCVW), pp 3765–3769

Jiang C, Bi M, Zhang S, et al (2024) Study on arc characteristics and combustion feature of tree-wire discharge fault in distribution line. Electric Power Systems Research 230:110210. https://doi.org/10.1016/j.epsr.2024.110210

Kim DK, Sunderland PB (2019) Fire ember pyrometry using a color camera. Fire Safety Journal 106:88–93. https://doi.org/10.1016/j.firesaf.2019.04.006

Manzello SL, Suzuki S, Gollner MJ, et al (2020) Role of firebrand combustion in large outdoor fire spread. Progress in Energy and Combustion Science 76:100801

Marxsen T (2015) Vegetation conduction ignition test report; final. Tech. rep., Marxsen Consulting Pty Ltd, URL https://discover.data.vic.gov.au/dataset/power

line-bushfire-safety-program-vegetation-conduction-ignition-test-report, accessed November 2016

Mell W, Jenkins M, Gould J, et al (2007) A physics-based approach to modelling grassland fires. International Journal of Wildland Fire 16:1–22. https://doi.org/10.1071/WF06002

Muhs JW, Parvania M, Nguyen HT, et al (2021) Characterizing probability of wildfire ignition caused by power distribution lines. IEEE Transactions on Power Delivery 36(6):3681–3688. https://doi.org/10.1109/TPWRD.2020.3047101

Ozansoy C, Sianaki OA (2024) Fire probability risk ranking of vegetation species in vegetation high impedance faults. International Journal of Electrical Power & Energy Systems 157:109804. https://doi.org/10.1016/j.ijepes.2024.109804

Sahila A, Boutchiche H, Viegas DX, et al (2023) A comparative study of the combustion dynamics and flame properties of dead Mediterranean plants. International Journal of Wildland Fire 32(6):979–988. https://doi.org/10.1071/WF22130

Thompson DK, Yip DA, Koo E, et al (2022) Quantifying firebrand production and transport using the acoustic analysis of in-fire cameras. Fire Technology 58(3):1617–1638. https://doi.org/10.1007/s10694-021-01194-y

Tse SD, Fernandez-Pello AC (1998) On the flight paths of metal particles and embers generated by power lines in high winds – a potential source of wildland fires. Fire Safety Journal 30(4):333–356

Victorian Government (2016) Powerline bushfire safety program; vegetation conduction ignition test report and data. https://discover.data.vic.gov.au/dataset/powerline-bushfire-safety-program-vegetation-conduction-ignition-test-report, accessed 22 July 2019

Wang X, Bocchini P (2023) Predicting wildfire ignition induced by dynamic conductor swaying under strong winds. Scientific Reports 13(1):3998. https://doi.org/10.1038/s41598-023-30802-w

Wunderlich AS, et al (2021) Protection scheme for fast detection and interruption of high-impedance faults on rate-limited DC distribution networks. IEEE Journal of Emerging and Selected Topics in Power Electronics 9(3):2540–2549. https://doi.org/10.1109/JESTPE.2020.2998056

Yang C, Zhang W, Tang R, et al (2025) Tree-related high-impedance fault in distribution systems: Modeling, detection, and ignition risk assessment (review). Energies 18(3):548. https://doi.org/10.3390/en18030548

Zen S, Thomas JC, Mueller EV, et al (2021) Development of a field deployable firebrand flux and condition measurement system. Fire Technology 57(3):1401–1424.

https://doi.org/10.1007/s10694-020-01074-x

Zhao Y, Wu S, Wang Y, et al (2023) Fire detection algorithm based on an improved strategy of YOLOv5 and flame threshold segmentation. Computers, Materials & Continua 75(3):5639–5657. https://doi.org/10.32604/cmc.2023.037829

Zhou T, Yuan T, Yang Q, et al (2025) Arc grounding fault model based on the dynamic characteristics of the entire process of distribution cherry tree related fault. Electric Power Systems Research 247:111781. https://doi.org/10.1016/j.epsr.2025.111781